Improved Vertical Carrier Transport for Green III-Nitride LEDs Using (In, Ga)N Alloy Quantum Barriers

Cheyenne Lynsky,[1,*,†] Guillaume Lheureux,[1,†] Bastien Bonef,[1] Kai Shek Qwah,[1] Ryan C. White,[1] Steven P. DenBaars,[1] Shuji Nakamura,[1] Yuh-Renn Wu,[2] Claude Weisbuch,[1,3] and James S. Speck[1]

[1] *Materials Department, University of California, Santa Barbara, California 93106, USA*

[2] *Graduate Institute of Photonics and Optoelectronics and Department of Electrical Engineering, National Taiwan University, Taipei 10617, Taiwan*

[3] *Laboratoire de Physique de la Matière Condensée, CNRS, IP Paris, Ecole Polytechnique, 91128 Palaiseau Cedex, France*

(Received 17 September 2021; revised 30 March 2022; accepted 20 April 2022; published 31 May 2022)

We report on experimental and simulation-based results using (In, Ga)N alloy quantum barriers in *c*-plane green light-emitting diode (LED) structures as a means to improve vertical carrier transport and reduce forward voltage (V_F). Three-dimensional device simulations that include random alloy fluctuations are used to understand carrier behavior in a disordered potential. The simulated current density–voltage (*J*-*V*) characteristics and modified electron-hole overlap $|F_{\mathrm{mod}}|^2$ indicate that increasing the indium fraction in the (In, Ga)N quantum barriers leads to a reduced polarization discontinuity at the interface between the quantum barrier and quantum well, thereby reducing V_F and improving $|F_{\mathrm{mod}}|^2$. Maps of electron and hole current through the device show a relatively homogenous distribution in the *XY* plane for structures using GaN quantum barriers; in contrast, preferential pathways for vertical transport are identified in structures with (In, Ga)N barriers as regions of high and low current. A positive correlation between hole (electron) current in the *p*-side (*n*-side) barrier and indium fraction reveals that preferential pathways exist in regions of high indium content. Furthermore, a negative correlation between the strain ε_{zz} and indium fraction shows that high indium content regions have reduced strain-induced piezoelectric polarization in the *Z* direction due to the mechanical constraint of the surrounding lower indium content regions. Experimentally, multiple quantum well green LEDs with (In, Ga)N quantum barriers exhibit lower V_F and blue-shifted wavelengths relative to LEDs with GaN quantum barriers, consistent with simulation data. These results can be used to inform heterostructure design of low V_F, long-wavelength LEDs and provide important insight into the nature of carrier transport in III-nitride alloy materials.

DOI: 10.1103/PhysRevApplied.17.054048

I. INTRODUCTION

Coherently grown [0001] oriented heterostructures consisting of (In, Ga)N quantum wells (QWs) and GaN quantum barriers (QBs) exhibit large internal electric fields due to discontinuities in total polarization at the QW/QB interface. Additionally, random compositional fluctuations in nitrides give rise to large potential energy fluctuations for carriers due to the large differences in band gaps between the constituent compounds, AlN, GaN, and InN. The spatially varying energy landscape at nanometer-length scales will modify the electrical and optical properties. As a result, alloy disorder strongly impacts carrier localization and transport in light-emitting diode (LED) devices [1–5]. These effects become more pronounced for green LEDs with high indium content (In, Ga)N QWs. It was recently demonstrated experimentally and through three-dimensional (3D) simulations based on the localization landscape (LL) theory of disorder that polarization barriers and band offsets at the GaN/(In, Ga)N (lower QB/QW) interface and sequential filling of QWs contribute to the large excess forward voltage in green III-nitride LEDs [6,7]. In addition to identifying a contributing factor to the low wall-plug efficiency of green LEDs, these findings highlighted the importance of using 3D as opposed to 1D simulations to accurately describe carrier transport in LEDs. A natural extension is the investigation of device structures that overcome these barriers to carrier transport in high indium composition QWs. In the work presented here, the impact of $In_xGa_{1-x}N$ quantum barriers on the electrical properties of green-emitting LEDs is examined experimentally and computationally. Structures incorporating $In_xGa_{1-x}N$ QBs will have a reduced polarization

*cheyennelynsky@gmail.com

†C. Lynsky and G. Lheureux contributed equally to this work.

discontinuity at the QW/QB interface and will also contribute an additional source of alloy disorder to the active region.

Kuo *et al*. previously explored the advantages of $In_{0.1}Ga_{0.9}N$ barriers in blue LEDs using APSYS simulations [8]. These authors propose that using (In, Ga)N barriers leads to more uniform electron and hole distribution in a multiple-quantum-well (MQW) structure resulting from the lower polarization discontinuity at the QW/QB interface. With more uniform carrier distribution, Auger recombination and thus efficiency droop are reduced. Experimentally, MQW blue LEDs with (In, Ga)N/(In, Ga)N QWs/QBs were demonstrated to have reduced efficiency droop, forward voltage, and wavelength shift with current compared to LEDs with GaN QBs [9]. Liu *et al*. also demonstrated that (In, Ga)N barriers led to improved carrier injection into deeper (*n*-side) QWs as evidenced by relative electroluminescence (EL) intensity of lower green-emitting QWs to a top blue-emitting QW [10].

Prior experimental reports motivate the use of (In, Ga)N barriers in *c*-plane green LEDs as a means of improving transport. To date, simulations performed on such structures have not accounted for the impact of alloy disorder in the (In, Ga)N barriers. Because compositional alloy fluctuations are a natural consequence of solid solutions and cannot be independently controlled in experiments, simulations present an attractive option for studying their impact on device performance. To understand carrier behavior in a disordered potential, full 3D treatment of the system is required. For this, we turn to a computational approach based on the LL theory of disorder to perform efficient 3D device simulations [11–14]. To simulate the electrical behavior of nitride-based devices, a Poisson-Schrödinger drift-diffusion solver should be used to solve the coupled equations self-consistently. To account for disorder-induced quantum effects, the Schrödinger equation should be solved in 3D for a disordered potential. However, self-consistently solving for the eigenstates in an alloy system using quantum mechanical calculations is too computationally demanding to be practical [14]. As an alternate approach, the LL model pioneered by Filoche and Mayboroda to obtain an equivalent semiclassical confining potential is applied here [11–13].

We present here an experimental and simulation-based study on the use of $In_xGa_{1-x}N$ quantum barriers in green-emitting III-nitride LEDs. Experimentally, we compare $In_{0.04}Ga_{0.96}N$ and GaN barriers on forward voltage in one-, three-, and five-QW green LEDs and perform characterization using atom probe tomography (APT). One- and two-QW LED structures with $In_xGa_{1-x}N$ barriers (where $x = 0$–0.05) are simulated using a 3D solver. From 3D simulations, we analyze the electrical device properties and the modified electron-hole overlap. Most importantly, we use simulation data to understand the role of random alloy fluctuations on carrier transport. The results presented here provide valuable, and to our knowledge previously unidentified, information regarding electron and hole transport through $In_xGa_{1-x}N$ alloy quantum barriers in an LED active region. In particular, we identify preferred current pathways through regions with high indium concentration originating from alloy disorder.

II. METHODS

To experimentally study the effect of alloy quantum barriers, green LEDs are grown by atmospheric pressure metalorganic chemical vapor deposition (MOCVD) on (0001) patterned sapphire substrates with either GaN or $In_{0.04}Ga_{0.96}N$ QBs and varying number of QWs. A low-temperature GaN nucleation layer is followed by 3 μm of unintentionally doped GaN, 2 μm of *n*-GaN, and a 45-period *n*-type (In, Ga)N/GaN superlattice. The active region is undoped and consists of 3-nm (In, Ga)N QWs, 2-nm $Al_{0.04}Ga_{0.96}N$ capping layers, and 8-nm GaN or $In_{0.04}Ga_{0.96}N$ QBs. Including (Al, Ga)N capping layers after the QW growth typically enables more aggressive GaN QB growth conditions, such as H_2 flow and high temperatures [15–18]. In the structures presented here, which use (In, Ga)N QBs, such aggressive growth conditions cannot be used as they prevent efficient indium incorporation. Nevertheless, (Al, Ga)N capping layers are standard in long-wavelength LED growth and are therefore included in the experimental structures. High resolution x-ray diffraction ω–2θ measurements of a thick (In, Ga)N calibration sample are performed on a Panalytical MRD PRO using Cu $K\alpha_1$ radiation ($\lambda = 1.5405$ Å) to calibrate the (In, Ga)N QB growth rate and composition. The LED active region has either one, three, or five QW periods. The *p*-side of the LED contains 10 nm of *p*+-GaN, 130 nm of *p*-GaN, and a 10-nm *p*+-GaN contact layer. A postgrowth anneal in N_2/O_2 at 600 °C for 15 min is used to activate the Mg-doped layers. LEDs are fabricated using standard mesa isolation and contact deposition. Pd/Au is used as the *p*-contact to GaN to allow for reliable voltage determination. APT measurements are performed on all samples to investigate the LED active region layer thicknesses and compositions. APT sample preparation, evaporation, and reconstruction details can be found in Ref. [19].

The *c*-plane green LED structure presented in Fig. 1(a) is used for the simulations. The single-QW structure consists of a 40-nm thick *n*-GaN layer (donor concentration $N_D = 5 \times 10^{18}$ cm^{-3}), a 3-nm $In_{0.22}Ga_{0.78}N$ QW, 7-nm $In_xGa_{1-x}N$ QBs on either side of the QW, and a 50-nm thick *p*-GaN layer (acceptor concentration $N_A = 2 \times 10^{19}$ cm^{-3}). The indium fraction x in the (In, Ga)N QB is varied from 0 to 0.05. The two-QW structure is identical to the one-QW structure, but an additional QW and QB are added to the active region. (Al, Ga)N capping layers are not used in these simulation structures. The (Al, Ga)N layers incorporated into the

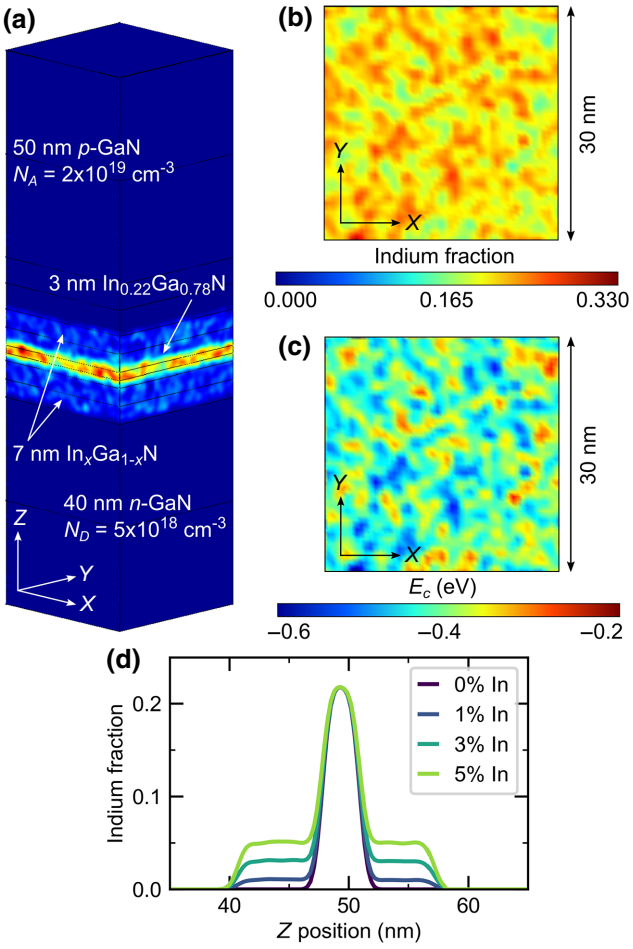

FIG. 1. (a) Full single-QW structure used in the simulations, where the color scale bar is given in (b). (b) *XY* map of indium distribution in the (In, Ga)N QW showing random lateral alloy fluctuations. (c) *XY* map of the conduction band potential $E_c(\mathbf{r})$ in the QW at a bias of 2.9 V. This map is the result of the compositional fluctuations in Fig. 1(b) and the associated variations in band gap, electric field, and carrier injection. (d) Indium alloy composition averaged in the *XY* plane along the *Z* direction for the four simulated structures with 22% indium in the QW and *x*% indium in the QBs, where $x = 0$, 1, 3, or 5.

experimentally grown samples are thin and contain a low aluminum fraction, as measured by APT. These layers are therefore not expected to strongly impact transport and are excluded from the simulations to avoid uncertainty in defining the complex (In, Ga)N/(Al, Ga)N/(In, Ga)N alloy profiles. Input parameters for each layer in the structure are provided in Table I. The LED structures are meshed using GMSH™ [20,21]. A constant mesh size of 0.6 nm is used in the *XY* planes and a variable mesh size is used in the *Z* direction, ranging from 1 nm in the *p*-GaN and *n*-GaN to 0.1 nm in the QWs and at the layer boundaries.

The indium alloy composition averaged in the *XY* plane along the *Z* direction is shown in Fig. 1(d) for all (In, Ga)N QB compositions used in the simulations. The composition profiles are based on those observed experimentally by APT [1,22]. In the 3D computations, the average indium composition of a layer is first defined, and a random number generator is used to assign indium and gallium atoms to each cation lattice site. The Gaussian averaging method described extensively in Ref. [14] is used to realize a continuous fluctuating composition. Figure 1(b) shows the random alloy map generated; the *XY* slice in the QW exhibits random alloy fluctuations as evidenced by the In-rich and In-poor regions. Although there are alloy fluctuations, the local band gap E_g is retained. The local alloy composition is used to assign the band gap E_g, dielectric constant ϵ_r, and effective mass m^* at each mesh node. The values of these parameters can be found in Table I of Ref. [14]. For an In$_x$Ga$_{1-x}$N alloy with indium fraction *x*, these parameters are determined by interpolating between GaN and InN according to the following equations

$$E_g^{\mathrm{In}_x\mathrm{Ga}_{1-x}\mathrm{N}} = (1-x)E_g^{\mathrm{GaN}} + xE_g^{\mathrm{InN}} - 1.4x(1-x), \quad (1)$$

$$\epsilon_r^{\mathrm{In}_x\mathrm{Ga}_{1-x}\mathrm{N}} = (1-x)\epsilon_r^{\mathrm{GaN}} + x\epsilon_r^{\mathrm{InN}}, \quad (2)$$

$$m^{*,\,\mathrm{In}_x\mathrm{Ga}_{1-x}\mathrm{N}} = [(1-x)/m^{*,\mathrm{GaN}} + xm^{*,\mathrm{InN}}]^{-1}. \quad (3)$$

The *XY* map of the conduction band potential $E_c(\mathbf{r})$ in the QW is shown in Fig. 1(c), where the conduction band offsets between GaN and (In, Ga)N are taken to be 63% of the band gap difference. However, the energy levels of electrons and holes are not given by the conduction and valence band potentials $E_{c,v}(\mathbf{r})$ as quantum effects occur due to the size and lateral dimensions of energy fluctuations. In the effective mass approximation, the true carrier energy levels are obtained by solving the Schrödinger equation obeyed by carriers in the fluctuating potential [14].

The 3D drift-diffusion charge control (3D DDCC) solver is employed here to perform device simulations [23,24]. In this model, the Schrödinger eigenvalue equation [Eq. (4)]

TABLE I. Simulation parameters used for each layer in the structure.

	n-GaN	(In, Ga) N QW	(In, Ga)N QB	*p*-GaN
Thickness (nm)	40	3	7	50
Doping (cm^{-3})	5×10^{18}	1×10^{17}	1×10^{17}	2×10^{19}
E_a (meV)	25			170
μ_e (cm^2/Vs)	200	300	300	32
μ_h (cm^2/Vs)	23	10	10	5
τ_n (s)	10	1×10^{-7}	1×10^{-7}	6×10^{-10}
τ_p (s)	7×10^{-10}	1×10^{-7}	1×10^{-7}	10
B_0 (cm^3/s)	2×10^{-11}	2×10^{-11}	2×10^{-11}	2×10^{-11}
C_0 (cm^6/s)	6×10^{-31}	6×10^{-31}	6×10^{-31}	6×10^{-31}

is replaced with the landscape equation [Eq. (5)]

$$\hat{H}\psi(\mathbf{r}) = E\psi(\mathbf{r}), \tag{4}$$

$$\hat{H}u_{e,h}(\mathbf{r}) = 1, \tag{5}$$

where the Hamiltonian for electrons and holes is given by

$$\hat{H} = -\frac{\hbar^2}{2m^*_{e,h}}\Delta + E_{c,v}(\mathbf{r}), \tag{6}$$

and ψ is the wave function, E is the eigenenergy, $u_{e,h}(\mathbf{r})$ are the electron and hole landscape functions, $m^*_{e,h}$ are the electron and hole effective masses, and $E_{c,v}(\mathbf{r})$ are the conduction and valence band potential energies. The semiclassical effective potentials $1/u_{e,h}(\mathbf{r})$ from LL theory capture quantum mechanical effects, such as carrier confinement [13]. By replacing an eigenvalue problem with a Dirichlet problem, self-consistently solving the coupled Poisson-landscape drift-diffusion equations becomes computationally tractable using the 3D DDCC solver [14].

Coherently grown III-N heterostructures in the [0001] orientation exhibit large internal electric fields resulting from discontinuities in spontaneous and piezoelectric polarization that must be accounted for in device simulations. A 3D continuum stress-strain model is solved using the finite element method to calculate the strain distribution. From the strain distribution, the strain-induced piezoelectric polarization $\mathbf{P}^{pz}$ can be evaluated by

$$\mathbf{P}^{pz} = [\mathbf{e}]\cdot[\varepsilon] = \begin{bmatrix} e_{15}\varepsilon_{xz} \\ e_{15}\varepsilon_{yz} \\ e_{31}(\varepsilon_{xx}+\varepsilon_{yy}) + e_{33}\varepsilon_{zz} \end{bmatrix}, \tag{7}$$

where ε_{xx}, ε_{yy}, ε_{zz} are normal strains and ε_{xy}, ε_{yz}, ε_{zx} are shear strains. e_{15}, e_{31}, e_{33} are the piezoelectric coefficients (Table II) from the piezoelectric tensor, where the other tensor terms are zero due to the 6mm point symmetry for the wurtzite crystal structure. The spontaneous polarization $\mathbf{P}^{sp}$ values, as related to the GaN buffer layer, are calculated from

$$\mathbf{P}^{sp} = ax + b(1-x) + cx(1-x), \tag{8}$$

where a, b, and c are coefficients given in Table II and x is the alloy composition of $In_xGa_{1-x}N$ or $Al_xGa_{1-x}N$. Taking the divergence of the total polarization $\mathbf{P}^{\text{total}}(\mathbf{r})$ over the entire domain, where $\mathbf{P}^{\text{total}}(\mathbf{r}) = \mathbf{P}^{pz} + \mathbf{P}^{sp}$, gives the induced fixed polarization charge $\rho_{\text{pol}}(\mathbf{r})$

$$\nabla\cdot\mathbf{P}^{\text{total}}(\mathbf{r}) = \rho_{\text{pol}}(\mathbf{r}). \tag{9}$$

The polarization-induced charge $\rho_{\text{pol}}(\mathbf{r})$ is solved once outside the self-consistency loop and is input into the Poisson equation to calculate the electrostatic potential $\varphi(\mathbf{r})$

TABLE II. Piezoelectric polarization coefficients for GaN, InN, and AlN and spontaneous polarization coefficients for (In, Ga)N and (Al, Ga)N alloys [25–27].

Piezoelectric	e_{15} (C cm^{-2})	e_{31} (C cm^{-2})	e_{33} (C cm^{-2})
GaN	−0.40	−0.49	0.73
InN	−0.40	−0.49	0.73
AlN	−0.48	−0.58	1.55
Spontaneous	a (C cm^{-2})	b (C cm^{-2})	c (C cm^{-2})
(In, Ga)N alloy	−0.042	−0.034	0.037
(Al, Ga)N alloy	−0.090	−0.034	0.021

and then $E_{c,v}(\mathbf{r})$. The electron and hole densities, n and p, respectively, are initially guessed. The Poisson equation is given by

$$\nabla\cdot(\varepsilon\nabla\varphi(\mathbf{r})) = e(n - p + N_A^- - N_D^+ \pm \rho_{\text{pol}}(\mathbf{r})), \tag{10}$$

where ε is the dielectric permittivity, e is the electron charge, and N_A^- and N_D^+ are the ionized acceptor and donor densities. After obtaining $E_{c,v}(\mathbf{r})$, the landscape equation [Eq. (5)] is solved for the landscape functions $u_{e,h}(\mathbf{r})$. The effective potentials $1/u_{e,h}(\mathbf{r})$ determine the bottom energy for the local density of states (LDOS, ρ) of the disordered system, which in landscape theory can be computed from Weyl's law in 3D [Eq. (11)] [13]. The carrier densities are then calculated from Eqs. (12) and (13)

$$\rho_{3D}(E,\mathbf{r}) = \frac{\sqrt{2}m^*_{e,h}}{\pi^2\hbar^3}\sqrt{|E - 1/u_{e,h}(\mathbf{r})|}, \tag{11}$$

$$n(E,\mathbf{r}) = \int_{1/u_e}^{+\infty}\rho_{3D}(E,\mathbf{r})f_n(E)dE, \tag{12}$$

$$p(E,\mathbf{r}) = \int_{-\infty}^{1/u_h}\rho_{3D}(E,\mathbf{r})f_p(E)dE, \tag{13}$$

where $f_n(E)$ and $f_p(E)$ are the Fermi-Dirac distributions for electrons and holes, respectively. The carrier densities are input into the drift-diffusion [Eqs. (14) and (15)] and recombination [Eqs. (16) and (17)] equations, which are given by the following

$$J_n = n\mu_n\nabla E_{F_n}, \tag{14}$$

$$J_p = p\mu_p\nabla E_{F_p}, \tag{15}$$

$$\nabla\cdot(J_{n,p}) = \pm e[A_0 + B_0np + C_0(n^2p + np^2)], \tag{16}$$

$$A_0 = \frac{np - {n_i}^2}{\tau_n(p + n_ie^{(E_i-E_t)/k_BT}) + \tau_p(n + n_ie^{(E_t-E_i)/k_BT})}. \tag{17}$$

J_n and J_p are the electron and hole current densities, μ_n and μ_p are the electron and hole mobilities, and E_{F_n} and E_{F_p} are the quasi-Fermi levels of electrons and holes. The

Shockley-Read-Hall (SRH) model is used to account for nonradiative recombination due to defects through the rate A_0 [Eq. (17)]. τ_n and τ_p are the nonradiative electron and hole lifetimes, n_i is the intrinsic carrier density, E_i is the intrinsic energy level, and E_t is the trap energy level, which is assumed to be at midgap. k_B is the Boltzmann constant and T is taken at room temperature. B_0 and C_0 are the radiative and Auger nonradiative recombination coefficients, respectively, of bulk materials without disorder or electric field (see Ref. [14] for a more complete discussion). In the computation, the electron-hole overlap is captured by locally calculating $n(\mathbf{r})$ and $p(\mathbf{r})$ [Eqs. (12) and (13)] and thus all recombination rates [Eqs. (16) and (17)].

In the simulation process, the spatial dependence of the total polarization $\mathbf{P}^{\text{total}}(\mathbf{r})$ is first calculated to obtain the fixed polarization charge $\rho_{\text{pol}}(\mathbf{r})$. Next, the Poisson equation is solved for the electrostatic potential $\phi(\mathbf{r})$ which is used to calculate $E_c(\mathbf{r})$ and $E_v(\mathbf{r})$. The landscape equations $\hat{H}u_e(\mathbf{r}) = 1$ and $\hat{H}u_h(\mathbf{r}) = 1$ are then solved for $u_e(\mathbf{r})$ and $u_h(\mathbf{r})$. From the effective potentials $1/u_e(\mathbf{r})$ and $1/u_h(\mathbf{r})$, the carrier densities of electrons and holes are calculated and fed back into the Poisson-drift-diffusion equations to be solved in a self-consistent manner. Convergence is achieved when the potential energy difference between two consecutive iterations is less than 10^{-5} eV.

III. RESULTS & DISCUSSION

A. *J-V* characteristics

Current density versus voltage (J-V) curves obtained from 3D DDCC simulations of the single-QW structure are plotted in Fig. 2(a) to explore the effect of (In, Ga)N QBs on forward voltage V_F. As the indium composition in the QBs is increased from 0% to 5%, V_F systematically decreases. At 35 A cm^{-2}, the voltage decrease is 0.05 V per one percent indium in the QB. The same curves for the two-QW structures with varying QB indium composition are shown in Fig. 2(b). Again, a decrease in voltage occurs with increasing indium fraction of the QB. For a given indium content, the two-QW structures exhibit higher forward voltage compared to the one-QW structures. This result agrees with prior experimental and simulation studies that show that for planar LEDs without engineered V-defects, additional QWs with undoped barriers are accompanied by a voltage penalty [6,7]. The source of the voltage penalty is assigned to polarization barriers and conduction band offsets at the QB/QW interface and sequential filling of QWs. Because the simulated structures used here are planar and do not contain a high density of V-defects, a voltage penalty with increasing QW number is expected.

While overall the two-QW structures present higher V_F than the one-QW structures, the decrease in V_F with increasing QB indium composition is also more significant. Here the voltage decrease per one percent indium in the QB is 0.11 V at 35 A cm^{-2}. The advantage of (In, Ga)N alloy QBs on electrical properties is therefore cumulative with increasing QW number. By increasing the indium fraction in the QB, the barrier to transport associated with each QW is decreased. For the 0% indium QB case, the voltage penalty for going from one to two QWs is 0.45 V; in contrast, the voltage penalty is only 0.22 V for the 5% indium QB structures. These results may be significant for commercial LEDs where large numbers of QWs are frequently used to improve the optical efficiency of LEDs but come with the drawback of worse electrical efficiency. (In, Ga)N QBs may provide a path to reduce the voltage penalty associated with increasing number of QWs.

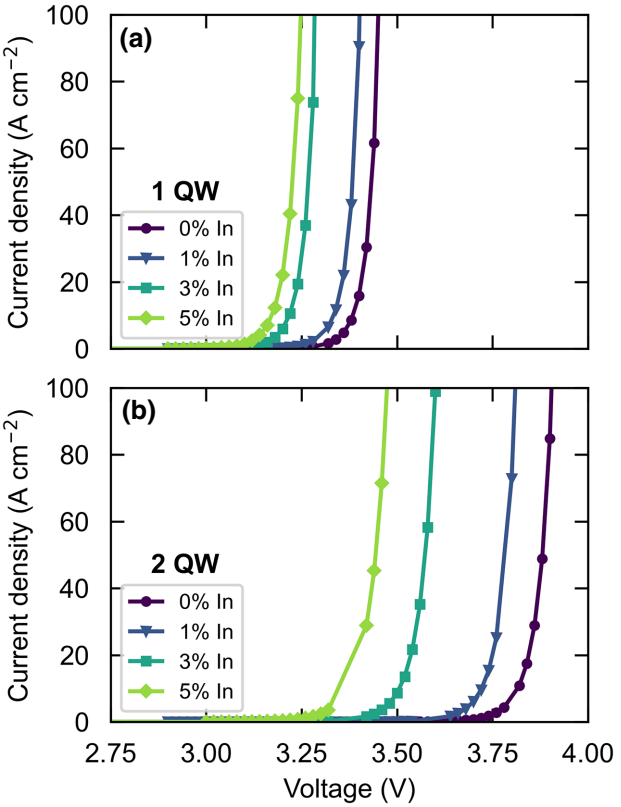

FIG. 2. J-V curves from 3D simulations of green LED structures with $In_xGa_{1-x}N$ quantum barriers of varying indium composition and either (a) one QW or (b) two QWs.

B. Carrier recombination

Simulations can also be used to assess the role of (In, Ga)N QBs on electron-hole recombination and hence provide additional insight into the reduction in V_F. Equation (16) shows the relationship between the recombination rates and current density. In the 3D DDCC simulations, $n(\mathbf{r})$ and $p(\mathbf{r})$ are computed in 3D for all $\mathbf{r}$ to calculate the SRH, radiative, and Auger recombination rates. Thus, the overlap of the carrier density is captured in the calculated n and p in the simulations. For a fixed

QW thickness and crystallographic orientation, an increase in wave function overlap in the Z direction at a given current density implies a reduced net electric field in the QW layer due to the flattening of the conduction and valence bands. Evaluating the electron-hole wave function overlap is therefore one way to assess recombination and electric fields in the QW.

Because the landscape equation is used here instead of the Schrödinger equation, the eigenvalues and eigenstates are not directly calculated. Instead, the carrier densities obtained in 3D are determined from the ρ assuming Weyl's law [Eqs. (11)–(13)] [13]. The normalized carrier densities for electrons and holes are calculated as follows:

$$n_{\text{norm}}(x,y,z) = \frac{n(x,y,z)}{\int_{x_1}^{x_2}\int_{y_1}^{y_2}\int_{z_1}^{z_2} n(x,y,z)\,dxdydz}, \tag{18a}$$

$$p_{\text{norm}}(x,y,z) = \frac{p(x,y,z)}{\int_{x_1}^{x_2}\int_{y_1}^{y_2}\int_{z_1}^{z_2} p(x,y,z)\,dxdydz}, \tag{18b}$$

$$\int_{x_1}^{x_2}\int_{y_1}^{y_2}\int_{z_1}^{z_2} n_{\text{norm}}(x,y,z)\,dxdydz = 1, \tag{19a}$$

$$\int_{x_1}^{x_2}\int_{y_1}^{y_2}\int_{z_1}^{z_2} p_{\text{norm}}(x,y,z)\,dxdydz = 1. \tag{19b}$$

The normalized densities are computed over the entire XY simulation domain. For the single-QW structure investigated here, Z_1 is chosen to be the middle of the n-side quantum barrier ($Z_1 = 45$ nm) and Z_2 to be the middle of the p-side quantum barrier ($Z_2 = 55$ nm). By defining the domain boundaries in this way, the carrier densities in the quantum barriers are considered, representing the wave function penetration in the barriers, which is largely increased due to compositional fluctuations. Normalization allows $n_{\text{norm}}(x,y,z)$ and $p_{\text{norm}}(x,y,z)$ to be treated as the probability of electron and hole presence in the Z_1 to Z_2 domain. $n_{\text{norm}}(x,y,z)$ and $p_{\text{norm}}(x,y,z)$ are then used to define the modified electron-hole overlap $|F_{\text{mod}}|^2$, a proxy for the square of the electron and hole wave function overlap $|F_{eh}|^2$, where

$$|F_{\text{mod}}|^2 = \left|\int_{x_1}^{x_2}\int_{y_1}^{y_2}\int_{z_1}^{z_2} \sqrt{n_{\text{norm}}(x,y,z)} \cdot \sqrt{p_{\text{norm}}(x,y,z)}\,dxdydz\right|^2. \tag{20}$$

$|F_{\text{mod}}|^2$ as a function of current density for the single-QW LED structure with different QB indium compositions is given in Fig. 3(a). In all cases, $|F_{\text{mod}}|^2$ increases with current density due to progressive carrier injection into the QW and subsequent reduction of the quantum confined Stark effect (QCSE) by partial screening of the electric field. For a given current density, $|F_{\text{mod}}|^2$ increases with increasing QB indium composition. This trend is attributed to a decrease in the net electric field in the QW resulting from the reduced polarization discontinuity at the QW/QB interface and reduced band offsets when using (In, Ga)N barriers as opposed to GaN barriers. With InN and GaN having similar spontaneous polarization coefficients but large lattice mismatch, the spontaneous polarization-induced electric field in the QW is small relative to the electric field arising from piezoelectric polarization.

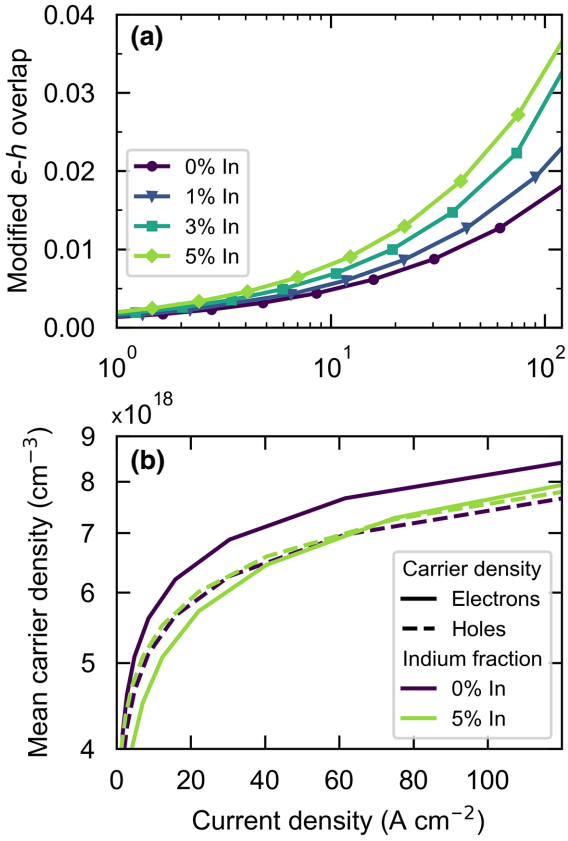

FIG. 3. Simulated dependence of (a) the modified electron-hole overlap $|F_{\text{mod}}|^2$ and (b) mean electron (solid) and hole (dashed) carrier density on current density for single-QW LEDs with different (In, Ga)N barrier compositions.

Increasing $|F_{\text{mod}}|^2$, and thus the recombination rate in the QWs, should also lead to a decrease in the steady-state carrier density at a given current density according to Eq. (16). To explore this, the mean electron and hole densities in the single-QW structure are computed according to Eq. (21),

$$\bar{n}(x,y,z) = \frac{\int_{x_1}^{x_2}\int_{y_1}^{y_2}\int_{z_1}^{z_2} n(x,y,z)\,dxdydz}{Z_2 - Z_1}, \tag{21a}$$

$$\bar{p}(x,y,z) = \frac{\int_{x_1}^{x_2}\int_{y_1}^{y_2}\int_{z_1}^{z_2} p(x,y,z)dxdydz}{Z_2 - Z_1}. \tag{21b}$$

The mean carrier densities are computed in the same domain as the normalized carrier densities. The dependence of $\bar{n}$ and $\bar{p}$ on current density for structures with different QB indium fraction are plotted in Fig. 3(b). In all cases, the mean carrier density increases sublinearly with injection current as n scales approximately between $J^{1/2}$ and $J^{1/3}$, following Eq. (16). As the indium fraction in the QB is increased, there is a very small change in $\bar{p}$ but a decrease in $\bar{n}$. With higher indium fraction in the QB, $|F_{\mathrm{mod}}|^2$ is increased [Fig. 3(a)] leading to faster recombination and reduced total carrier density [Fig. 3(b)].

A change in $|F_{\mathrm{mod}}|^2$ is expected to impact the dependence of internal quantum efficiency (IQE) on current density, where the IQE is defined as the ratio of the radiative recombination rate to the recombination rate due to all processes. Figure 4(a) shows the IQE curves for single-QW structures. While the peak IQE is similar for all structures, with higher QB indium fraction a slight increase in the current density at peak IQE and a significant reduction in droop are observed. The improvement in droop behavior can be explained by the lower steady-state carrier density and therefore reduced Auger rate ($C_0(n^2p + np^2)$) relative to the radiative rate (B_0np). An additional impact on carrier recombination is seen when looking at the fraction of current due to carrier overflow from the QW at higher currents, computed as the difference between the injected current and the recombination currents. It is shown in Fig. 4(b) that at a given current density, the overflow fraction of current is smaller for structures with higher indium fraction in the barrier and that overflow becomes negligible for LEDs with 3% and 5% indium. This trend can be better understood by plotting the dependence of overflow fraction on the ratio of the applied voltage V to the built-in GaN p-n diode voltage V_{BI} (V_{BI}= 3.3 V) with $N_D = 5 \times 10^{18}$ cm^{-3} and $N_A = 2 \times 10^{19}$ cm^{-3} (assuming 1% acceptor ionization). These results are shown in Fig. 4(c) where the curves for different QB indium fractions closely overlay one another. From the data in Figs. 4(b) and 4(c), it is observed that the overflow current is a result of applying a bias in excess of V_{BI}. This emphasizes that carrier overflow becomes significant only when V exceeds V_{BI} of the GaN p-n junction and that overflow is not connected to the turn-on voltage of the LED. Therefore, incorporating (In, Ga)N QBs in green LED structures not only reduces the forward voltage but also leads to lower carrier overflow. To further avoid overflow current at high diode voltages, an (Al, Ga)N electron blocking layer should be used. In Fig. 4(d), the dependence of the Auger fraction of current on V/V_{BI} is shown. Unlike overflow, there is an appreciable fraction of Auger at $V/V_{\mathrm{BI}} < 1$, a regime where droop is observed in Fig. 4(a). The Auger fraction then begins to decrease with increasing V/V_{BI} as a smaller fraction of carriers are injected in the QW, corresponding to the increase in carrier overflow. At $V/V_{\mathrm{BI}} = 1.05$, overflow and Auger have approximately

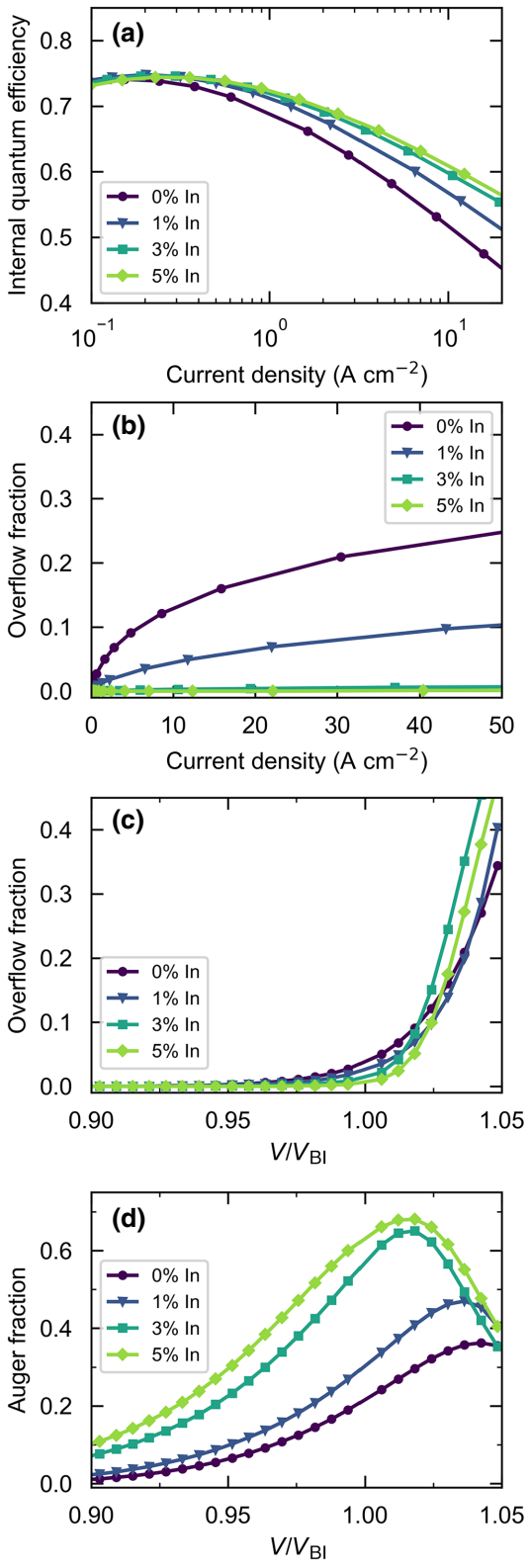

FIG. 4. Simulated dependence of (a) internal quantum efficiency (IQE) at low current densities and (b) overflow fraction of current density for single-QW LED structures. (c) Overflow fraction dependence on the ratio of applied voltage V to built-in diode voltage V_{BI}, where $V_{\mathrm{BI}} = 3.3$ V. (d) Auger fraction dependence on V/V_{BI}.

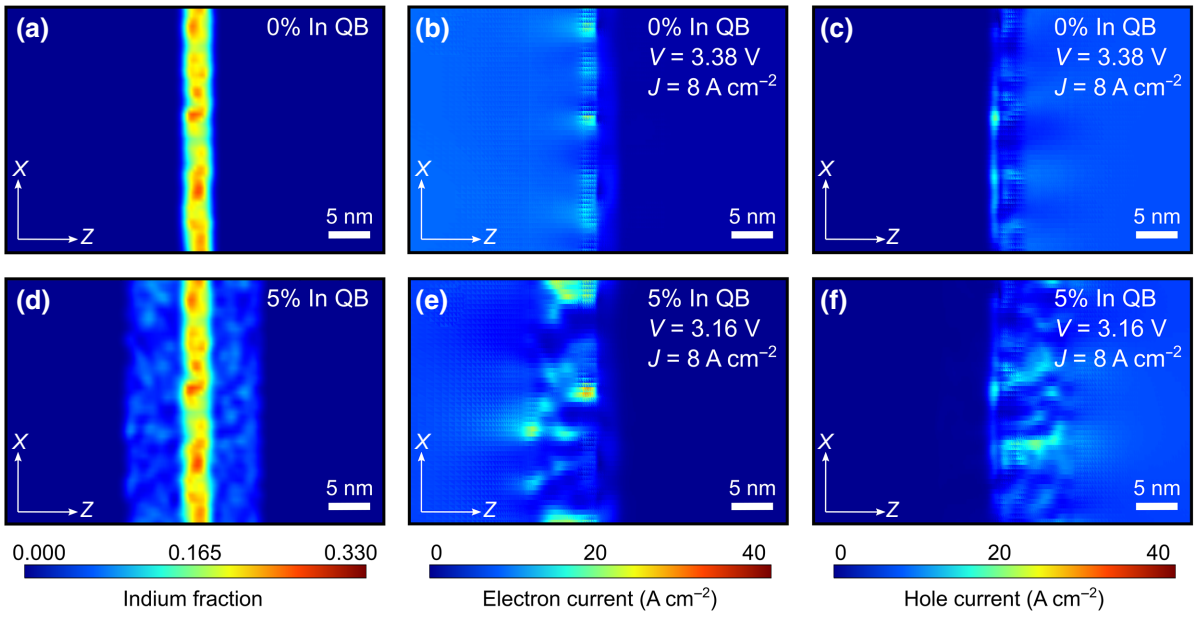

FIG. 5. The *XZ* plane (a) indium composition map, (b) electron current density map, and (c) hole current density map for a one-QW LED with 0% indium barriers. The *XZ* plane (d) indium composition map, (e) electron current density map, and (f) hole current density map for a one-QW LED with 5% indium barriers. It can be seen that the high indium composition quantum barrier structure results in high electron and hole current pathways.

the same contribution to the total current and therefore to droop.

C. Percolative pathways

3D simulations allow for the determination of the percolative transport paths in III-nitride materials that arise due to random alloy fluctuations. Comparing structures with GaN and (In, Ga)N barriers, spatial differences in electron current can be visualized. Figure 5 shows indium, electron current, and hole current maps in the *XZ* plane for one-QW structures with either GaN or $In_{0.05}Ga_{0.95}N$ quantum barriers. The (In, Ga)N composition maps for the GaN and $In_{0.05}Ga_{0.95}N$ QB structures are shown in Figs. 5(a) and 5(d), respectively. At a current density of 8 A cm^{-2}, high electron current [Fig. 5(e)] and hole current [Fig. 5(f)] pathways are observed for the structure with (In, Ga)N barriers. In contrast, the electron current [Fig. 5(b)] and hole current [Fig. 5(c)] are more homogeneous for the GaN QB structure and do not show the same regions of extreme high and low current. The inhomogeneous current maps indicate a secondary effect of (In, Ga)N barriers in addition to the average reduced polarization discontinuity at the QW/QB interface. From the current maps

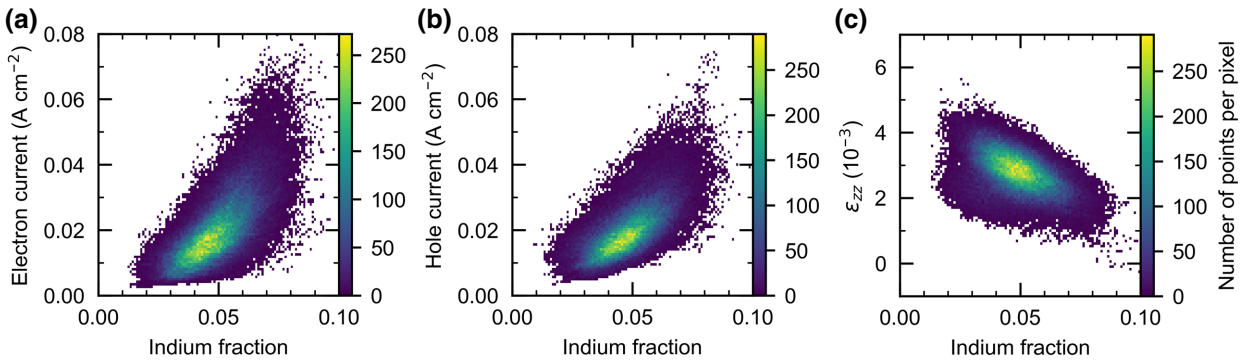

FIG. 6. Correlation plots for the one-QW LED structure with 5% indium barriers (a) Electron current density $|J_n|$ as a function of the indium composition in the *n*-side QB and (b) hole current density $|J_p|$ as a function of the indium composition in the *p*-side QB at $V = 2.9$ V, below V_{BI}. Both the electron and hole current densities are higher in regions of high indium composition. (c) *Z* component normal strain ε_{zz} as a function of indium composition. ε_{zz} decreases with indium composition in the QB.

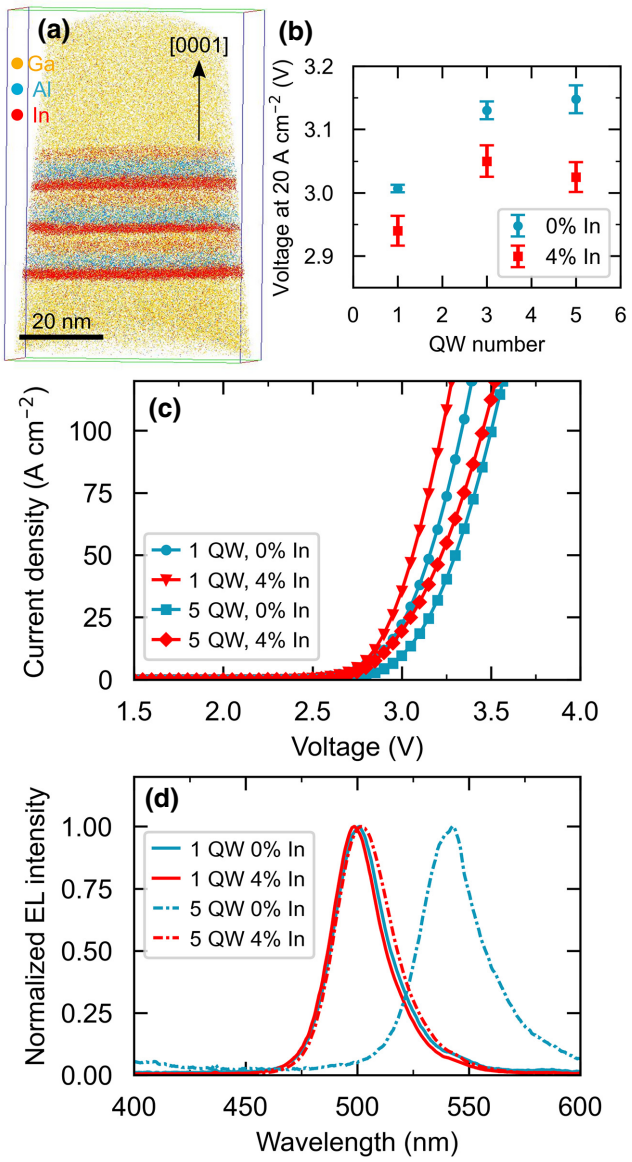

FIG. 7. (a) Atom probe tomography 3D reconstruction of the active region of a three-QW LED with 4% indium (In, Ga)N quantum barriers. (b) Experimental V_F measured at 20 A cm^{-2} for LEDs with one, three, or five QWs and either 0% or 4% indium (In, Ga)N QBs. A reduction in V_F is measured for LED structures with (In, Ga)N quantum barriers. (c) J-V curves and (d) electroluminescence (EL) spectra for LEDs with one or five QWs and 0% or 4% indium (In, Ga)N quantum barriers.

it is clear that there are preferential paths for carriers to flow through the barrier layers to then inject the QW. Alloy disorder, introduced through the addition of indium to the QB, is a likely explanation for the spatial variation in current through the structure. It is then of interest to identify what nanoscale variations in materials properties lead to the altered carrier transport.

To further explore the role of alloy fluctuations and percolative pathways on carrier transport, the magnitude of electron current $|J_n|$ in the n-side QB and the magnitude of hole current $|J_p|$ in the p-side QB are plotted as a function of indium composition in Figs. 6(a) and 6(b), respectively, for each computational node in the QBs. We note here that scatter plots obtained using $|J_n|$ and $|J_p|$ are nearly identical to those using J_{nz} and J_{pz}, respectively. For both the n-side and p-side QBs, nodes are taken in the full 30 nm $\times$ 30 nm XY plane. The n-side QB domain is defined from $Z = 41$ to $Z = 47$ nm for a total number of 150 858 nodes and the p-side QB domain is defined from $Z = 52$ to $Z = 57$ nm for a total of 124 828 nodes. The scatter plots in Fig. 6 show the properties associated with each simulation node in the given domain. Here, the average indium fraction of the QB is fixed at 0.05 and the variations from approximately 0.02 to 0.08 represent the random alloy fluctuations for a simulation node. A positive correlation is observed between electron current in the n-side barrier and indium fraction as well as hole current in the p-side barrier and indium fraction. This correlation indicates that the favorable path for carriers to transport through (In, Ga)N quantum barriers is along the regions of high indium content. This can in part be understood by considering the reduced conduction and valence band offsets in regions of high QB indium composition. However, another factor that should also be examined is the effect of alloy composition on strain, and therefore strain-induced piezoelectric polarization $\mathbf{P}^{pz}$.

A scatter plot of the dependence of the Z-component normal strain ε_{zz} on indium composition in the quantum barrier is given in Fig. 6(c). The domain shown is for the p-side QB from $Z = 52$ to $Z = 57$ nm; however, similar results are obtained for the n-side QB. The average ε_{zz} is approximately 3×10^{-3} and a negative correlation is observed where ε_{zz} decreases with increasing indium fraction in the p-side QB. At first this result may seem counterintuitive; typically for a uniform alloy, a larger ε_{zz} would be expected for a higher indium composition (In, Ga)N film strained to an underlying GaN lattice. However, a random alloy (In, Ga)N film with regions of high and low indium composition is being considered here. The regions of high indium composition will exhibit a smaller ε_{zz} as the lattice is constrained in the Z direction by the surrounding low indium composition regions. Conversely, the low indium compositions will have a larger ε_{zz} due to the surrounding regions of high indium composition. A correlation plot of ε_{zz} as a function of indium fraction for the one-QW structure with 1% indium QBs (not shown here) gives the same negative correlation; however, the average ε_{zz} is less than the average ε_{zz} for the 5% indium QB structure, which is qualitatively the expected trend. The negative correlation between ε_{zz} and indium fraction in the QB, for a structure with a fixed average indium fraction, indicates that areas of higher indium content have a relatively lower Z component of $\mathbf{P}^{pz}$. The high indium composition, low $\mathbf{P}^{pz}$, regions may further provide

favorable, low barrier pathways for carriers to transport through the QBs and into the QWs. This agrees with previous results showing that polarization discontinuities at the QW/QB interface result in a polarization barrier for carrier transport and thus excess voltage in green LEDs [7].

D. Experimental measurements

To compare the simulation and experimental trends, the grown samples are characterized to identify whether the trend of lower voltage with (In, Ga)N barriers is observed. Figure 7(a) shows the APT reconstruction of the active region of the three-QW LED with (In, Ga)N barriers. The three (In, Ga)N QWs, (Al, Ga)N capping layers, and (In, Ga)N QBs can be clearly observed in this 3D reconstruction. The indium and aluminum concentrations measured in APT are consistent with those expected from growth calibrations. From the profiles, a decrease in the indium fraction at the top side of the (In, Ga)N QB is observed. This thin layer can be explained by unintentional indium desorption from the QB during the growth pause (to allow for the substrate temperature to decrease) before the QW growth. A more uniform indium fraction in the QB could be achieved in future growths by reducing this growth pause.

The six green LEDs are measured under electrical injection to elucidate the impact of alloy quantum barriers on electrical device properties. Consistent with simulations, for all samples, a decrease in forward voltage is observed for (In, Ga)N barriers relative to GaN barriers. The voltage at 20 A cm^{-2} for all LEDs are shown in Fig. 7(b) and the full J-V curves for representative one- and five-QW LEDs are shown in Fig. 7(c). For both the (In, Ga)N and GaN QB LEDs, V_F first increases from one to three QWs but remains constant from three to five QWs. Previous results on c-plane green LEDs with GaN QBs showed a large voltage increase with increasing QW number due to polarization-related barriers to carrier transport [6]. The moderate increase in voltage with QW number here is attributed to the use of a high period (In, Ga)N/GaN superlattice and a low aluminum fraction (Al, Ga)N capping layer. LEDs from previous studies that showed a large voltage penalty used a ten-period superlattice and a 20% aluminum cap layer, whereas the structures reported here incorporate a 45-period superlattice and a 4% aluminum cap layer. The high period (In, Ga)N/GaN superlattice leads to the nucleation of inverted hexagonal pyramid defects, known as V-defects [28–31]. The role of V-defects in reducing the QW-QB polarization barriers is supported by recent literature on long-wavelength III-nitride LEDs which showed that V-defects may provide a path for carrier injection into the QWs via the semipolar sidewall, thus leading to lower V_F [32–35]. In the present study, the V-defect density is approximately 2×10^8 cm^{-3}, which is below the frequently cited optimal V-defect density value of around 1×10^9 cm^{-3} that leads to substantial improvements in V_F [35]. Therefore, the V-defects are hypothesized to lead to a reduction in the voltage penalty, but the effect would be too small to render the simulation and experimental structures incomparable. Additionally, high aluminum fraction (Al, Ga)N capping layers have been shown to contribute a voltage penalty [16]. The reduced aluminum fraction used here is also expected to result in a lower voltage penalty with each additional QW.

Accounting for the difference in superlattice period and therefore V-defect density, the experimental trend of reduced V_F with (In, Ga)N QBs is consistent with the simulation results. In addition, the peak EL wavelength is blue shifted for LEDs with (In, Ga)N barriers, likely due to the reduced polarization discontinuity at the lower QB/QW interface and therefore reduced QCSE. The EL spectra for the one- and five-QW LEDs with 0% and 4% indium QBs are shown in Fig. 7(d). The peak EL wavelengths for the one-, three-, and five-QW samples with GaN barriers are 505, 515, and 541 nm, respectively. The peak EL wavelengths for the one-, three-, and five-QW samples with (In, Ga)N barriers are 500, 498, and 500 nm, respectively. A blue shift with decreasing QW number for the GaN barrier samples is also observed. This is attributed to an increase in the residual electric field of the p-n junction (due to a decrease in active region width), which cancels out a portion of the polarization-related electric field in the QW. The result is a decrease in the net electric field across the QW and a blue shift as the QCSE is reduced.

IV. CONCLUSION

From our analysis of 3D simulation results, which capture random alloy fluctuations and their associated effects, we find that (In, Ga)N alloy quantum barriers provide several advantages over GaN quantum barriers. Using (In, Ga)N barriers not only reduces the polarization discontinuity at the QB/QW interface, leading to improved modified electron-hole overlap $|F_{\text{mod}}|^2$ and reduced V_F, but also provides favorable pathways for carriers to inject the QWs. For a single-QW structure with 5% indium in the QB, we observe that regions with higher indium content have higher electron current in the n-side barrier, higher hole current in the p-side barrier, and lower ε_{zz}. The high indium fraction regions therefore provide preferential pathways for carrier transport as a result of the lower Z component of the strain-induced piezoelectric polarization. Consistent with the simulation data, LED structures grown by MOCVD with (In, Ga)N quantum barriers also exhibit lower V_F than those with GaN barriers. The findings presented here highlight the role of alloy disorder on carrier transport and overall device behavior as well

as demonstrate the importance of the 3D treatment of III-nitride materials and devices in simulations.

ACKNOWLEDGMENTS

This work was supported by the U.S. Department of Energy under Award No. DE-EE0008204, the National Science Foundation under Grant No. DMS-1839077, grants from the Simons Foundation (Grant No. 601952, J.S. and Grant No. 601954, C.W.), Sandia National Laboratory (Grant No. 2150283), by the Solid State Lighting and Energy Electronic Center (SSLEEC), and by the Taiwanese Ministry of Science and Technology (MOST) under Grant No. MOST 108-2628-E-002-010-MY3. This work was supported by the international collaborative project TECCLON, funded by the French Agence Nationale de la Recherche (ANR), Grant No. ANR-20-CE05-0037-01, and the by the Taiwanese MOST, Grant No. MOST 111-2923-E-002-009. This work made use of the central facilities supported by the NSF MRSEC Program of the NSF under Grant No. DMR 11-21053; a member of the NSF-funded Materials Research Facilities Network. A portion of this work was performed in the UCSB Nanofabrication Facility, an open access laboratory.

[1] T.-J. Yang, R. Shivaraman, J. S. Speck, and Y.-R. Wu, The influence of random indium alloy fluctuations in indium gallium nitride quantum wells on the device behavior, J. Appl. Phys. **116**, 113104 (2014).

[2] D. A. Browne, B. Mazumder, Y.-R. Wu, and J. S. Speck, Electron transport in unipolar InGaN/GaN multiple quantum well structures grown by NH3 molecular beam epitaxy, J. Appl. Phys. **117**, 185703 (2015).

[3] W. Hahn, *et al.*, Evidence of Nanoscale Anderson Localization Induced by Intrinsic Compositional Disorder in InGaN/GaN Quantum Wells by Scanning Tunneling Luminescence Spectroscopy, Phys. Rev. B **98**, 045305 (2018).

[4] R. Aleksiejūnas, K. Nomeika, O. Kravcov, S. Nargelas, L. Kuritzky, C. Lynsky, S. Nakamura, C. Weisbuch, and J. S. Speck, Impact of Alloy-Disorder-Induced Localization on Hole Diffusion in Highly Excited c-Plane and m-Plane (In, Ga)N Quantum Wells, Phys. Rev. Appl. **14**, 054043 (2020).

[5] K. S. Qwah, M. Monavarian, G. Lheureux, J. Wang, Y.-R. Wu, and J. S. Speck, Theoretical and experimental investigations of vertical hole transport through unipolar AlGaN structures: Impacts of random alloy disorder, Appl. Phys. Lett. **117**, 022107 (2020).

[6] C. Lynsky, A. I. Alhassan, G. Lheureux, B. Bonef, S. P. DenBaars, S. Nakamura, Y.-R. Wu, C. Weisbuch, and J. S. Speck, Barriers to Carrier Transport in Multiple Quantum Well Nitride-Based c-Plane Green Light Emitting Diodes, Phys. Rev. Mater. **4**, 054604 (2020).

[7] G. Lheureux, C. Lynsky, Y.-R. Wu, J. S. Speck, and C. Weisbuch, A 3D simulation comparison of carrier transport in green and blue c-plane multi-quantum well nitride light emitting diodes, J. Appl. Phys. **128**, 235703 (2020).

[8] Y.-K. Kuo, J.-Y. Chang, M.-C. Tsai, and S.-H. Yen, Advantages of blue InGaN multiple-quantum well light-emitting diodes with InGaN barriers, Appl. Phys. Lett. **95**, 011116 (2009).

[9] J. Xu, *et al.*, Reduction in efficiency droop, forward voltage, ideality factor, and wavelength shift in polarization-matched GaInN/GaInN multi-quantum-well light-emitting diodes, Appl. Phys. Lett. **94**, 011113 (2009).

[10] J. P. Liu, J.-H. Ryou, R. D. Dupuis, J. Han, G. D. Shen, and H. B. Wang, Barrier effect on hole transport and carrier distribution in InGaN/GaN multiple quantum well visible light-emitting diodes, Appl. Phys. Lett. **93**, 021102 (2008).

[11] M. Filoche and S. Mayboroda, Universal mechanism for Anderson and weak localization, PNAS **109**, 14761 (2012).

[12] M. Filoche, M. Piccardo, Y.-R. Wu, C.-K. Li, C. Weisbuch, and S. Mayboroda, Localization Landscape Theory of Disorder in Semiconductors. I. Theory and Modeling, Phys. Rev. B **95**, 144204 (2017).

[13] D. N. Arnold, G. David, D. Jerison, S. Mayboroda, and M. Filoche, Effective Confining Potential of Quantum States in Disordered Media, Phys. Rev. Lett. **116**, 056602 (2016).

[14] C.-K. Li, M. Piccardo, L.-S. Lu, S. Mayboroda, L. Martinelli, J. Peretti, J. S. Speck, C. Weisbuch, M. Filoche, and Y.-R. Wu, Localization Landscape Theory of Disorder in Semiconductors. III. Application to Carrier Transport and Recombination in Light Emitting Diodes, Phys. Rev. B **95**, 144206 (2017).

[15] Y.-L. Hu, *et al.*, Effect of quantum well cap layer thickness on the microstructure and performance of InGaN/GaN solar cells, Appl. Phys. Lett. **100**, 161101 (2012).

[16] T. Shioda, H. Yoshida, K. Tachibana, N. Sugiyama, and S. Nunoue, Enhanced light output power of green LEDs employing AlGaN interlayer in InGaN/GaN MQW structure on sapphire (0001) substrate, Phys. Status Solidi A **209**, 473 (2012).

[17] A. I. Alhassan, R. M. Farrell, B. Saifaddin, A. Mughal, F. Wu, S. P. DenBaars, S. Nakamura, and J. S. Speck, High luminous efficacy green light-emitting diodes with AlGaN cap layer, Opt. Express **24**, 17868 (2016).

[18] A. I. Alhassan, N. G. Young, R. M. Farrell, C. Pynn, F. Wu, A. Y. Alyamani, S. Nakamura, S. P. DenBaars, and J. S. Speck, Development of high performance green c-plane III-nitride light-emitting diodes, Opt. Express **26**, 5591 (2018).

[19] B. Bonef, M. Catalano, C. Lund, S. P. Denbaars, S. Nakamura, U. K. Mishra, M. J. Kim, and S. Keller, Indium segregation in n-polar InGaN quantum wells evidenced by energy dispersive x-ray spectroscopy and atom probe tomography, Appl. Phys. Lett. **110**, 143101 (2017).

[20] C. Geuzaine and J.-F. Remacle, Gmsh: A three-dimensional finite element mesh generator with built-in pre- and post-processing facilities, Int. J. Numer. Methods Eng. **79**, 1309 (2009).

[21] See http://gmsh.info/ for more information about GMSH, a three-dimensional finite element mesh generator.

[22] Y.-R. Wu, R. Shivaraman, K.-C. Wang, and J. S. Speck, Analyzing the physical properties of InGaN multiple quantum well light emitting diodes from nano scale structure, Appl. Phys. Lett. **101**, 083505 (2012).

[23] C.-K. Wu, C.-K. Li, and Y.-R. Wu, Percolation transport study in nitride based LED by considering the random alloy fluctuation, J. Comput. Electron. **14**, 416 (2015).
[24] See http://yrwu-wk.ee.ntu.edu.tw/ for "Optoelectronic device simulation laboratory".
[25] A. E. Romanov, T. J. Baker, S. Nakamura, and J. S. Speck, Strain-induced polarization in wurtzite III-nitride semipolar layers, J. Appl. Phys. **100**, 023522 (2006).
[26] V. Fiorentini, F. Bernardini, and O. Ambacher, Evidence for nonlinear macroscopic polarization in III–V nitride alloy heterostructures, Appl. Phys. Lett. **80**, 1204 (2002).
[27] O. Ambacher, *et al.*, Pyroelectric Properties of Al(In)GaN/GaN Hetero- and quantum well structures, J. Phys.: Condens. Matter **14**, 3399 (2002).
[28] B. Heying, E. J. Tarsa, C. R. Elsass, P. Fini, S. P. DenBaars, and J. S. Speck, Dislocation mediated surface morphology of GaN, J. Appl. Phys. **85**, 6470 (1999).
[29] X. H. Wu, C. R. Elsass, A. Abare, M. Mack, S. Keller, P. M. Petroff, S. P. DenBaars, J. S. Speck, and S. J. Rosner, Structural origin of V-defects and correlation with localized excitonic centers in InGaN/GaN multiple quantum wells, Appl. Phys. Lett. **72**, 692 (1998).
[30] M. Shiojiri, C. C. Chuo, J. T. Hsu, J. R. Yang, and H. Saijo, Structure and formation mechanism of V defects in multiple InGaN/GaN quantum well layers, J. Appl. Phys. **99**, 073505 (2006).
[31] I.-H. Kim, H.-S. Park, Y.-J. Park, and T. Kim, Formation of V-shaped pits in InGaN/GaN multiquantum wells and bulk InGaN films, Appl. Phys. Lett. **73**, 1634 (1998).
[32] Z. Quan, L. Wang, C. Zheng, J. Liu, and F. Jiang, Roles of V-Shaped pits on the improvement of quantum efficiency in InGaN/GaN multiple quantum well light-emitting diodes, J. Appl. Phys. **116**, 183107 (2014).
[33] C.-K. Li, C.-K. Wu, C.-C. Hsu, L.-S. Lu, H. Li, T.-C. Lu, and Y.-R. Wu, 3D numerical modeling of the carrier transport and radiative efficiency for InGaN/GaN light emitting diodes with V-shaped pits, AIP Adv. **6**, 055208 (2016).
[34] F. Jiang, *et al.*, Efficient InGaN-based yellow-light-emitting diodes, Photonics Res. **7**, 144 (2019).
[35] S. Zhang, *et al.*, Efficient emission of InGaN-based light-emitting diodes: Toward orange and red, Photonics Res. **8**, 1671 (2020).